In vitro and *in vivo* phasor analysis of stoichiometry and pharmacokinetics using near-infrared dyes

Authors

Sez-Jade Chen[1*], Nattawut Sinsuebphon[1*], Alena Rudkouskaya[2], Margarida Barroso[2], Xavier Intes[1], Xavier Michalet[3†]

Affiliations

[1]*Department of Biomedical Engineering, Rensselaer Polytechnic Institute, Troy, NY, 12180, USA*
[2]*Department of Molecular and Cellular Physiology, Albany Medical College, Albany, NY, 12208, USA*
[3]*Department of Chemistry and Biochemistry, University of California Los Angeles, Los Angeles, CA, 90095, USA*
* These authors contributed equally to this work
†Corresponding author

1 Abstract

We introduce a simple new approach for time-resolved multiplexed analysis of complex systems using near-infrared (NIR) dyes, applicable to *in vitro* and *in vivo* studies. We first show that fast and precise *in vitro* quantification of NIR fluorophores lifetime and stoichiometry can be done using phasor analysis, a computationally efficient and user-friendly representation of complex fluorescence intensity decays obtained with pulsed laser excitation. We apply this approach to the study of binding equilibria by Förster resonant energy transfer (FRET), using two different model systems: primary/secondary antibody binding *in vitro* and ligand/receptor binding in cell cultures. We then extend our demonstration to dynamic imaging of the pharmacokinetics of transferrin binding to the transferrin receptor in live mice, elucidating the kinetic of differential transferrin accumulation in specific organs, straightforwardly differentiating specific from non-specific binding. Our method, implemented in a freely-available software package, has all the advantages of time-resolved NIR imaging, including better tissue penetration and background-free imaging, but simplifies and considerably speeds up data processing and interpretation, while remaining quantitative. These advances make this method attractive and of broad applicability for *in vitro* and *in vivo* molecular imaging, and could be extended to applications as diverse as image guided-surgery or optical tomography.

2 Introduction

Molecular imaging enables the characterization and quantification of biological processes in live and intact subjects[1-5]. The ability to monitor, with high spatial and temporal resolution, biological processes *in vivo* and longitudinally has been central to improving our knowledge of integrative biology, more sensitive and specific means to characterize diseases, guiding the development of novel therapies and/or rationalizing therapeutic regimen selection, as well as dynamically assessing treatment efficacy. The most important characteristics sought in molecular imaging techniques are the ability to sense minute amounts of molecules as well as being able to simultaneously track various markers in the same tissue. In this regard, Positron Emission Tomography (PET) is the main molecular imaging technique for diagnosis and study in human clinical trials thanks to its high sensitivity, and it is likewise common for preclinical studies. Despite its widespread use, one of the main drawbacks of PET is that the information provided by the pooling of the

injected radiotracers can be nonspecific if the tracer is not well-targeted, such as for the clinically-approved marker FDG (Fluodeoxyglucose) for tracking of metabolic activity[6]. The sensitivity of PET can also be highly dependent upon the tracer itself and its efficacy of delivery within the body with regards to metabolism and clearance of the tracer[5], and the use of radiotracers limits its potential for longitudinal studies. Lastly, it is difficult to perform PET multiplexing studies (track multiple biomarkers) *in vivo*. Conversely, optical imaging techniques demonstrate in preclinical settings similar levels of sensitivity to PET with the advantage of being able to use a wide array of fluorescence reporters, including genetically-encoded reporters. Though molecular optical imaging has been historically mainly limited to *in vitro* and preclinical work, there has been a surge in the last decade in the development of optical imaging techniques for clinical applications ranging from guided surgery to medical intervention.

Molecular optical imaging methods harness information provided by light reflected from or transmitted through tissues, as well as emitted fluorescence or luminescence from probes (exogenous or endogenous) within the tissue. A wide array of functionalized fluorophore libraries has been developed over the years to permit tracking numerous molecular processes or biomarkers of interests *in vitro* and *in vivo*. However, in the case of *in vivo* applications, optical imaging of intact tissue does not provide cellular or intra-cellular resolution and hence, like PET, is limited to macro- or meso- localization of the fluorescent probe[7,8]. Thus, for applications involving delivery of molecular probes, such as in targeted drug delivery, only reporting of the probe pooling at the tissue level is possible. This is particularly an issue in oncological applications in which vascular delivery of probes harnesses the enhanced permeability and retention (EPR) effect[9,10] but does not guarantee intracellular delivery.

In contrast, fluorescence lifetime is a property of a fluorophore (whether exogenous or endogenous), which is mostly independent of concentration but is sensitive to changes to the microenvironment such as pH or ion concentration[11,12]. In addition, quantitative lifetime imaging is a powerful tool to monitor nanoscale biological interactions via Förster Resonance Energy Transfer (FRET), a phenomenon in which an excited fluorophore (the 'donor') transfers energy non-radiatively to a nearby fluorophore (the 'acceptor') provided they have sufficient spectral overlap and are 2-10 nm apart[13,14]. This results in a decrease in donor fluorescence emission intensity and lifetime due to quenching, and an increase in the acceptor intensity. Quantification of this change in the donor lifetime provides direct information on the FRET interaction.

Fluorescence lifetime imaging (FLI) has proven to be a robust tool *in vitro* and *in vivo* for observation of contrast within biological tissues. Lifetime imaging is well-established in microscopy and in the visible range of the spectrum, but its application *in vivo* is technically challenging due to significant and diverse background auto-fluorescence and high signal attenuation in tissues. These limitations can be mitigated by using NIR or longer wavelength emitting species, due to reduced scattering and absorption[15]. However, to quantitatively retrieve lifetime or lifetime-based quantities, model-based analysis is required and usually involves fitting algorithms. Iterative fitting approaches typically used are computationally demanding and can be an obstacle to fast quantitative imaging, as needed in some clinical applications such as guide surgery or to study fast *in vivo* kinetics. For such applications, the availability of fast quantitative tools for quantitative lifetime imaging is still lacking. Herein, we report on the development of a fast computational tool, based on phasor analysis, to retrieve quantitatively, accurately and in close to real-time, the lifetime and lifetime-based quantities over whole images. In particular, we illustrate our approach with the case of small animal whole-body *in vivo* NIR FRET imaging.

NIR FRET is a promising approach to observe cellular interactions *in vivo* and to assess drug delivery efficacy. In this study, we utilize the transferrin/transferrin receptor (Tf/TfR) pair as a model of ligand/receptor binding interaction. Tf is a blood plasma glycoprotein acting as an iron transporter and binding to TfR. TfR is highly expressed in the liver, which is the main organ regulating iron homeostasis, but also in cancerous tissue[16]. This makes Tf an attractive carrier for targeted therapy[17], as binding of two drug-carrying Tf molecules to the receptor dimer results in endocytosis and delivery of the drug into the cell[18,19]. Here,

we use NIR donor and acceptor dyes conjugated to Tf to probe Tf/TfR receptor-ligand dimerization and internalization process *in vivo*. Due to the close proximity of the TfR binding sites within the dimer, the donor- and acceptor-labeled Tf experience FRET upon binding and internalization, resulting in a reduced (quenched) donor lifetime[20,21]. The detection of a quenched donor lifetime by FLI within a region of interest thus directly reports on Tf delivery into the cells, as we recently verified *in vivo*[22-24].

Standard analysis of FLI-FRET data typically consists of fitting the fluorescence lifetime decay in each pixel to a multi-exponential model[25,26]. This subsequently allows for extraction of FRET parameters such as the FRET efficiency and the fraction of donor quenched due to FRET within the sample. However, fluorescence decay fitting analysis can be time-consuming and fraught with problems when applied to large images with limited signal-to-noise ratio. Alternative methods such as rapid lifetime determination (RLD[27]) and minimal fraction of interacting donor[28] have been developed to circumvent these limitations, but these methods have not been tested with short-lifetime NIR dyes in the presence of broad impulse response function (IRF) such as encountered in *in vivo* measurements[29]. In these situations, an approach such as phasor analysis that does not rely on specific decay models and does not focus on extracting lifetimes, could be particularly useful due to its speed and ease of use as demonstrated next[30-40].

Phasor (or polar plot) analysis of fluorescence lifetime images (phFLI) was initially introduced as a simple and graphical way to represent data acquired with frequency-modulated systems[31,41]. The method can be used as well with fluorescence lifetime data acquired with other modalities, such as scanning confocal time-correlated single photon-counting (TCSPC)[33], wide-field time-gated[34] or wide-field photon-counting[42] detection and others[43]. Briefly, the method consists in transforming the recorded fluorescence

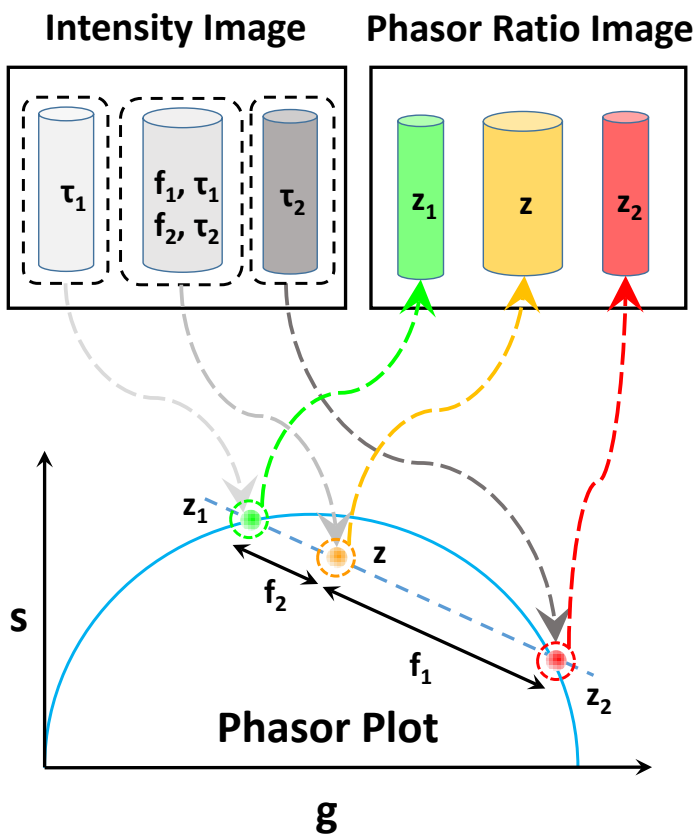

Figure 1: Principle of phasor analysis. Fluorescence lifetime data can be represented with almost no processing as an intensity image (top left panel). The phasor representation of this data (easily calculated for each pixel with equation (SI-1) (supplementary information) can be displayed as a phasor plot (gray arrows and bottom panel), in which pixels characterized by similar fluorescence decays are clustered together around the universal circle (UC, blue), where pure exponential decays are located. This representation then allows the selection of clusters of phasors (e.g. cluster z_1: green, z_2: red and z: orange) and highlighting the corresponding pixels of the image with different colors (colored arrows and top right panel). In the example schematically shown here (top left), samples with lifetime τ_1 and τ_2, and a mixture of both (fractions f_1 and f_2), the samples phasors z_1 and z_2 are located on the UC, while the mixture's phasor z is located on the line connecting them. In this type of cases, it is simple to compute and color-code, almost in real-time, the fraction f_1 of sample 1 (also called phasor ratio) in the original image. The resulting "phasor ratio image" is thus a convenient "map" of the fraction of the lifetime of interest within the sample. Quantitative analysis can also be performed, as discussed in the main text and supplementary information.

decay *F(t)* into a pair of numbers (*g, s*) proportional to the Fourier transform of *F* at a chosen frequency *f*, or equivalently the complex number $z = g + is$, the so-called *phasor*, defined by:

$$z = g + is = \int_0^\infty dtF(t)\, e^{i2\pi ft} \Big/ \int_0^\infty dtF(t) \ , \tag{1}$$

f, the *phasor harmonic*, is typically chosen equal to a small integer multiple of the laser repetition frequency. The (*g*, *s*) pair is then represented in a two-dimensional plot, the so-called *phasor plot*, whose properties are summarized in figure 1 and in supplementary note 2. A particularly useful property of the phasor representation is that the phasor *z* of a single-exponential decay is located on the so-called *universal circle*, with short lifetimes at one end ($\tau = 0 \rightarrow z = 1$) and long lifetime at the other ($\tau = \infty \rightarrow z = 0$). All other single exponential decays are located in between, as expressed by SI equation (SI-7). Due to the linearity of the Fourier transform, the phasor of a mixture of species is equal to a linear combination of their individual phasors, the weight factor of each species being equal to its emitted intensity (SI equation (SI-18))[33]. The phasor representation of an image, which comprises the phasor of each pixel, is easily computed and represented graphically as a 2-dimensional histogram in the phasor plot. Such a representation allows visual identification of molecular species characterized by distinct fluorescence decays, without any assumption about the underlying decay model function. Following identification of different species of interest in the phasor plot (figure 1), the corresponding sources (*i.e.* image pixels) can be immediately located in the original image. Using color-coding, each identified species can be mapped in a false-color overlay image, allowing rapid identification of a sample's lifetime heterogeneity. Finally, precise quantification of the respective fractions of two or more components can be performed, provided the location of known species' phasor location can be determined.

This method has been successfully applied in a number of *in vitro* studies using fluorophores emitting in the visible range of the spectrum and characterized by fluorescence lifetimes that are long compared to the width of the instrument response function (IRF)[35-40] Importantly, these studies have so far been exclusively performed *in vitro* where very little scattering takes place.

In this work, we demonstrate that phasor analysis can be successfully used in the challenging situation presented by short lifetime NIR dyes, even in the presence of the broad IRF encountered during *in vivo* experiments. We first demonstrate that small NIR lifetime changes (20 ps) can be readily detected and quantified by phasor analysis, even though the intrinsic lifetimes of these dyes are very short. We next build on this result to show that mixtures of short NIR lifetimes can be quantified *in vitro*, using first a pair of distinct dyes mixed at different ratios. We then extend this demonstration to a single dye exhibiting different lifetimes due to FRET, in two different *in vitro* FRET-based binding assays. Finally, we extend our demonstration to *in vivo* studies by studying the kinetics of transferrin engagement with the transferrin receptor in live mice. We conclude that the quantitative nature, ease of use and interpretation, as well as rapid data acquisition and analysis afforded by the phFLI approach, make it a very powerful new molecular imaging method for *in vitro* as well as *in vivo* real time kinetic studies.

3 Results

3.1 Accurate measurement of short NIR lifetimes

We first characterized the ability of NIR phFLI to precisely quantify the short fluorescence lifetimes which are typical of most NIR dyes, by taking advantage of the exquisite sensitivity of lifetime on specific environmental perturbations. In this and all subsequent experiments, we used a time-gated fluorescence lifetime imaging system described in previous publications (and in supplementary methods)[44]. Since we used it in most of our experiments, we characterized Alexa Fluor 700 (AF700), which has a reported lifetime of 1 ns in water. Like many dyes, such as dyes from the oxazine family, AF700 exhibits a larger lifetime in organic solvents (for instance ethanol, EtOH) than in aqueous buffers (for instance phosphate buffered

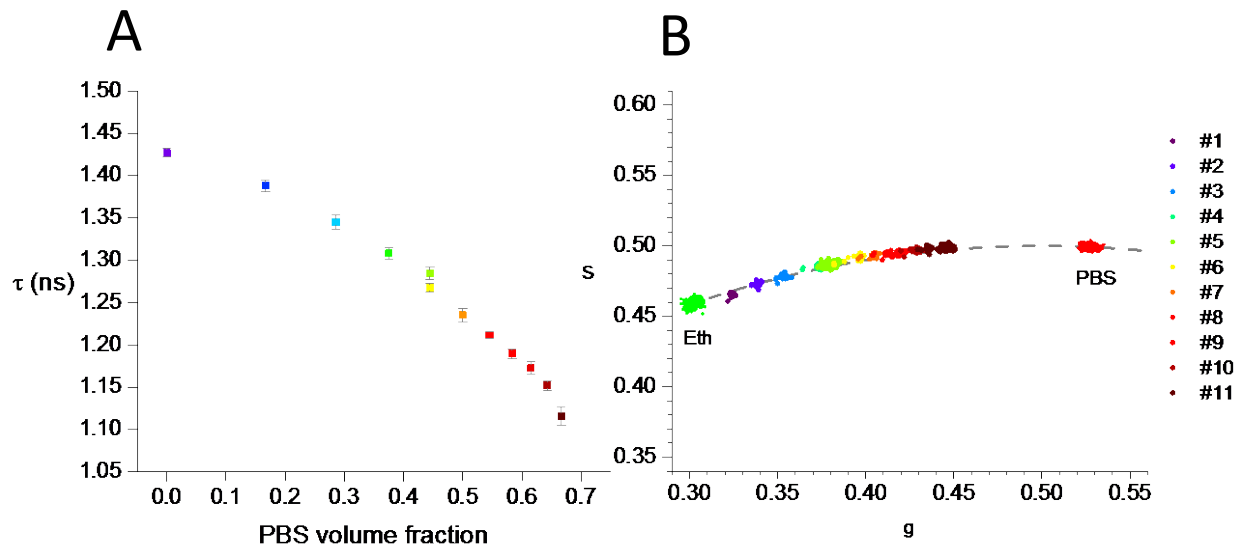

Figure 2: Phase lifetime (A) and phasor (B) of AF700 in EtOH:PBS as a function of PBS volume fraction. A: Each point corresponds to the average of 20 measurements (*). The error bar shows the standard deviation for each mixture. The measurable changes in lifetimes from one condition to the next range from 17 to 43 ps, with a typical standard deviation within each measurement of 10 ps. The instrument response function's FWHM was 177 ± 7 ps. (*) Points 5+6 and 11 correspond to the average of 100 measurements. B: Detail of the phasor graph showing the corresponding phasors for each individual measurement (noted #n) as well as for the samples in pure ethanol (left, green) and pure PBS (right, red), used as reference for calibration. Clusters for each dilution are readily separated. Some small temporal evolution of the sample is clearly visible during each series of measurements. Additional details in online Methods, supplementary figure 1 and movie 1.

saline, PBS)[45,46]. The lifetime of AF700 can thus be modulated in a predictable manner by changing the ratio of EtOH to PBS in the solution. Figure 2A-B and supplementary movie 1 show the changes in the phase lifetime of AF700 (supplementary information (SI) equation (SI-7)) and phasor as different amounts of PBS were added to a 100 µL EtOH solution of AF700. Lifetime steps of 20 ps or less are clearly identifiable. Similar results were obtained using different starting solutions and dilution sequences (supplementary figure 1A-B), consistent with quenching of AF700's fluorescence by PBS (supplementary figure 1C). Importantly, the extracted phase lifetimes (obtained by phasor analysis) were comparable to the lifetimes obtained by a standard single-exponential fitting approach (supplementary figure 1D), although they were performed completely independently from one another.

3.2 Analysis of mixtures of NIR species characterized by different lifetimes

Having established the ability of phFLI to measure short fluorescence lifetimes of individual NIR dyes, we studied *mixtures* of NIR dyes characterized by *similar* emission spectra but *different* lifetimes and asked how reliably the *fraction* of each species can be measured by phFLI. The ability to quantify the amount of fluorophores differing only by their lifetime would allow using lifetime as a contrast mechanism, and open up the possibility to use it to analyze molecular interactions by FRET.

In traditional lifetime fitting approaches, assuming that each component of a mixture is characterized by a distinct, single exponential decay, a simple definition of the fraction of each component is given by the relative amplitude α_i of each exponential component of the mixture's decay (SI equation (SI-24)). Alternatively, the phasor z of a mixture of different species, which is simply a weighted sum of each individual species' phasor z_i (SI equation (SI-18)):

$$z = f_1 z_1 + f_2 z_2 , \tag{2}$$

leads to a natural definition of each species' fraction as the phasor weight f_i of this species. As explained in figure 1 and in supplementary note 2, if the phasors of each isolated species are known (for instance from separate measurements of each individual dye), f_i is given by the relative distance of the sample's phasor to that species' phasor (the so-called *phasor ratio*, SI equation (SI-20)-(SI-21)):

$$f_1 = (z - z_2)\frac{(z_1 - z_2)^*}{|z_1 - z_2|^2}. \tag{3}$$

α_i and f_i can be used interchangeably if the two lifetimes of the reference species are known (SI equation (SI-25)). These quantities can be connected to independently measurable observables such as the species' *volume fraction* v (SI equation (SI-35)), *number fraction* n (SI equation (SI-37) or *concentration ratio* M (SI equation (SI-33)), by simple expressions involving a single parameter χ characterizing the dyes photo-physical properties and instrument sensitivity (SI equation (SI-30)) and the initial concentration ratio μ of the two dyes (SI equation (SI-34)):

$$f_1^{-1} - 1 = (\chi\mu)^{-1}\left(v_1^{-1} - 1\right). \tag{4}$$

In particular, μ can be chosen such that $f(v)$ becomes linear.

Figure 3 shows the results of phasor analysis of different mixture series of various initial concentrations of ATTO 740 (A740) and 1,1′,3,3,3′,3′-Hexamethylindotricarbocyanine iodide (HITCI), two NIR dyes which can both be excited at 740 nm and emit around 770 nm, and are characterized by different lifetimes in PBS buffer (A740: 567 ± 11 ps, HITCI: 356 ± 4 ps). Each series corresponds to variable volume fractions v_1 of HITCI (species 1, initial concentration $[\text{HITCI}]_0$) and A740 (species 2, initial concentration $[\text{A740}]_0$), and is fully characterized by the ratio μ of their initial concentrations. As predicted by SI equation (SI-35), the phasor ratios of each series depend only on μ and the volume fractions v_1, the dependence becoming

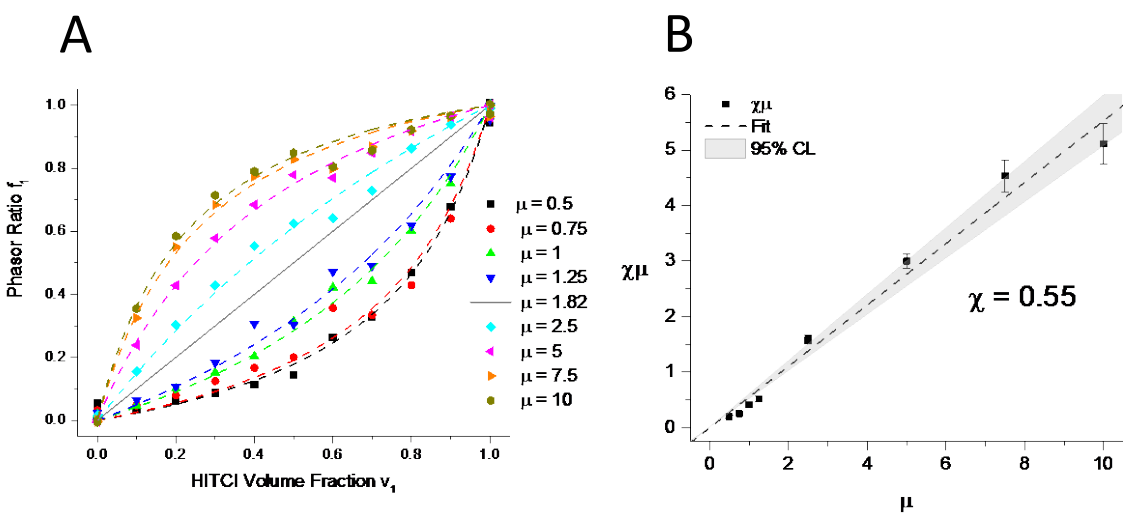

Figure 3: Analysis of series of mixtures of dyes with different lifetimes. A: Phasor ratio of different series of mixtures of ATTO 740 and HITCI. Each series is characterized by a variable volume fraction v_1 of HITCI, v_1 = 0, 0.1,…, 0.9, 1 and initial concentration ratio $\mu = [\text{HITCI}]_0/[\text{A740}]_0$ given in the legend. Each data series is fitted with the theoretical expression for $f_1(v_1)$ discussed in the text, yielding a parameter value $\chi\mu$ studied in B. B: Relation between $\chi\mu$ (obtained from the analysis described in A) and μ. A linear dependence is verified, with χ = 0.55.

linear for a single value $\mu = \chi^{-1}$. Importantly, the lifetime fitting analysis performed independently provides identical results (supplementary figure 2).

In other words, knowing χ and the lifetimes of the two dyes, it is possible to recover the volume fraction in any mixture based on the measurement of the phasor ratio f. These results demonstrate the ability of phFLI analysis to provide quantitative information on the composition of mixtures of species characterized by similar emission spectra (and therefore undistinguishable spectroscopically) but different lifetimes.

3.3 Analysis of *in vitro* NIR FRET

The ability to distinguish identical dyes differing only by their lifetime is, in particular, useful for the analysis of binding equilibria by FRET. In this application, the association of two molecules, one of which is labeled with a donor dye and the other with an acceptor dye, is detected by energy transfer of the donor

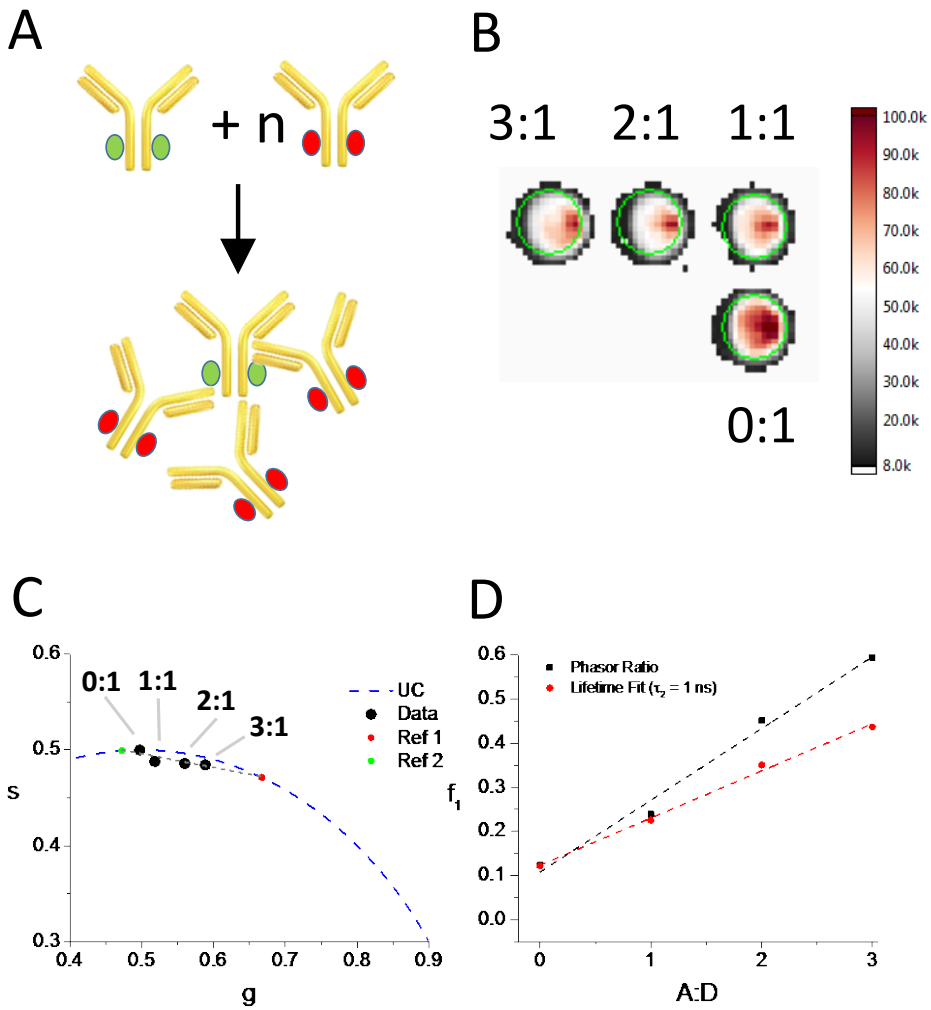

Figure 4: *in vitro* analysis of IgG pair interaction. A: Principle of the experiment. N-fold amounts of acceptor-labeled secondary IgG (red) are added to a fixed amount of donor-labeled primary IgG (green), to form secondary/primary IgG complexes. B: Resulting samples are analyzed with time-gated imaging (shown are the total intensity images, summing all time-gate images). C: Phasor analysis of each sample, once calibrated with the known lifetime of the pure donor sample (0:1), shows alignment of the different phasors. The two limiting values correspond to the pure donor sample (0:1, green), and a hypothetical, fully quenched sample (red) with lifetime τ_{DA} = 703 ps). D: Representation of the phasor ratio f_1 (black squares) for these samples, demonstrating a linear dependence on the A:D ratio, in reasonable agreement with the results obtained by lifetime fitting (red circles).

to the acceptor. In the absence of binding, no FRET occurs and the measured donor lifetime is simply the unquenched donor lifetime τ_{D0}. In the case of binding, FRET between donor and acceptor results in a decreased lifetime τ_{DA}. If the bound donor-acceptor configuration is unique, the FRET efficiency (hence the FRETing donor lifetime τ_{DA}) is a constant and τ_{DA} can be considered as the second reference lifetime of the mixture of bound and unbound donor molecules. Measurement of the fractions of the fluorescence decay with lifetime τ_{D0} or τ_{DA} is then equivalent to measuring the respective fraction of unbound and bound donor respectively, and thus allows full characterization of the binding equilibrium. This can be challenging to do using multi-exponential fits, in particular when short lifetimes are involved, but as discussed in the next two examples, this is straightforward using phFLI analysis.

3.3.1 Quantification of FRET between IgG antibodies

In the first example, schematically depicted in figure 4A, known amounts of donor-labeled mouse primary antibody (AF700-IgG) were mixed with increasing amounts of acceptor-labeled goat anti-mouse secondary antibody (AF750-IgG). When increasing the acceptor-labeled to donor-labeled IgG ratio (A:D), the average number of AF750-IgG molecules bound to each AF700-IgG molecule increases, resulting in more FRET interactions and thus a larger fraction of donor molecules involved in FRET. As discussed above, these changes are reflected in the donor fluorescence decay, and have previously been measured by time-gated fluorescence imaging and lifetime fitting analysis[44]. Here, time-gated imaging data was analyzed by phFLI and compared to the corresponding fluorescence decay fitting results.

Figure 4C represents the series of phasor locations for these different A:D ratios. They are clearly aligned along a segment connecting the donor-only phasor located on the universal semicircle (green dot), and another intersection with the semicircle (red dot), identified with the hypothetical maximally quenched donor. Figure 4D shows the observed linear dependence of the phasor ratio as a function the A:D ratio (black squares), as predicted by the simple model discussed in supplementary note 4, despite the multiplicity of lifetimes involved in this system. This result agrees qualitatively well with the corresponding short lifetime fraction extracted by standard bi-exponential lifetime fitting analysis (red circles), which is not expected to perform well in the presence of potentially more than two lifetimes, showing that phFLI can quantitatively report on the equilibrium association between FRET binding partners *in vitro*.

3.3.2 Quantification of FRET receptor-ligand binding in cells

A particularly important example of molecular interactions that can be studied by FRET methods is that of ligand-receptor binding in cells. Many such interactions are implicated in signal transduction pathways, and represent a major target of drug development [47]. Although labeled antibodies (such as used in the experiments discussed above) can be used for cell studies of ligand-receptor binding[48], a more effective approach available when receptor dimers exist, consists in using labeled ligands. By labeling a fraction of the externally delivered ligands with a donor molecule (D) and another fraction with an acceptor molecule (A), it is then possible to quantify the fraction of doubly-labeled (D + A) receptors by FRET. As in the previous example using labeled antibodies, measurements can be done by time-gated donor lifetime measurements and analyzed by phFLI (figure 5 and supplementary note 5 for theoretical details).

In a large range of situations, the predicted doubly-labeled equilibrium fraction depends simply on the initial A:D ratio. phFLI analysis of donor fluorescence then enables plotting the expected phasor of the mixture as a function of the initial A:D ratio and, with appropriate reference values, the FRET fraction. Two distinct regimes can be identified: (i) one in which the FRET fraction increases to asymptotically reach a maximum value, and (ii) another where the FRET fraction varies linearly with the A:D ratio. Both regimes are of practical relevance: the first regime is that observed in *in vitro* cell measurements discussed in this section, while the second regime is relevant for the *in vivo* experiments described in the next section.

We used holo-transferrin (Tf), an iron-binding blood plasma glycoprotein commonly used as drug carrier[49], and the transferrin receptor (TfR1), a receptor typically overexpressed in cancer cells and the liver.

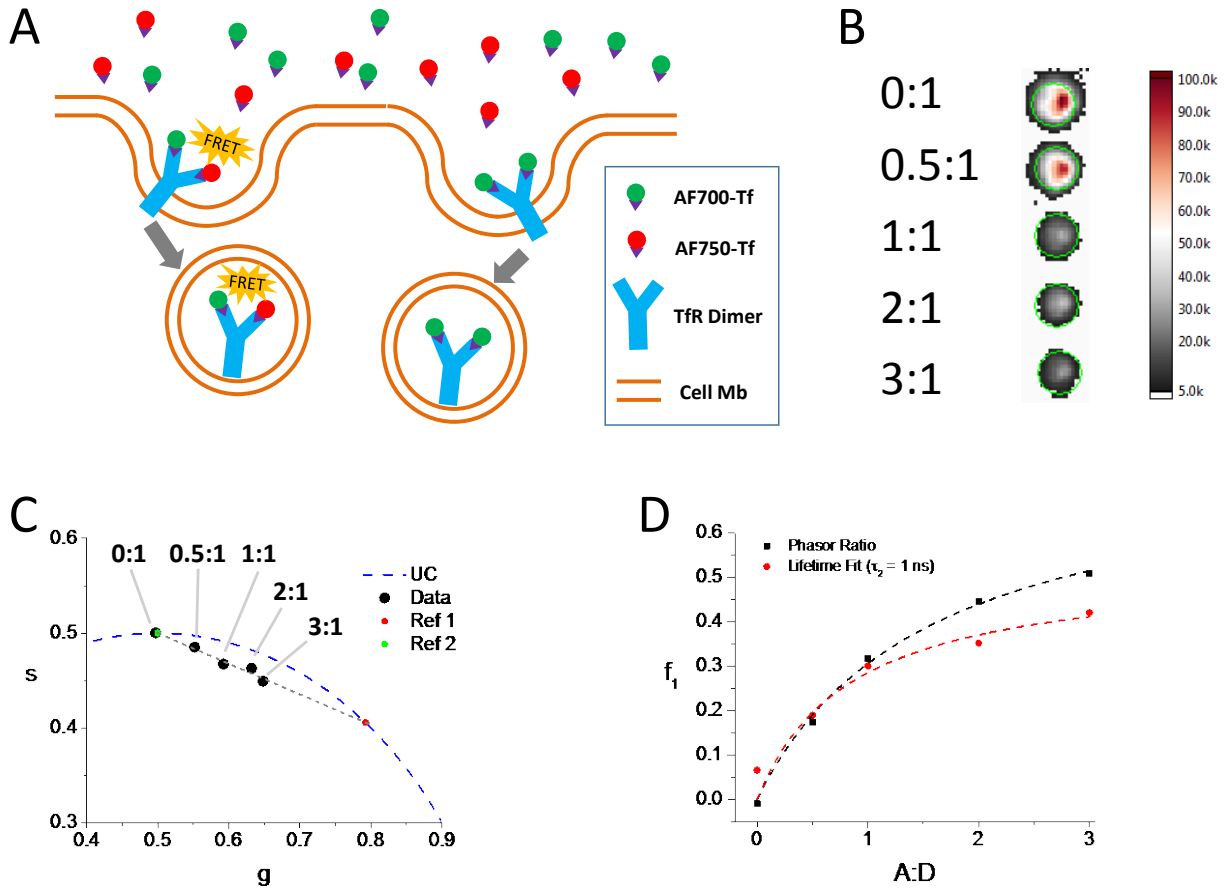

Figure 5: *in vitro* analysis of transferrin receptor (TfR) engagement by transferrin (Tf). A: Principle of the experiment. Different amounts of acceptor-labeled (red) or donor-labeled Tf (green) were added to T47D cells expressing TfR on their surface, leading to Tf binding and TfR internalization by endocytosis. B: Total intensity images of fixed T47D cell cultures incubated with varying ratios (A:D) of acceptor- to donor-labeled Tf. C: Phasor analysis of each sample, once calibrated with the known lifetime of the pure donor sample (0:1), shows alignment of the different phasors. The two limiting values correspond to the pure donor sample (0:1, green), and a maximally quenched donor (red) with lifetime τ_{DA} = 509 ps). D: Representation of the phasor ratio f_1 showing increase and saturation as a function of A:D ratio (black square). The corresponding quantity obtained by lifetime fitting analysis is shown for comparison (red circle). Both agree qualitatively but differ due to the different lifetimes extracted by global fitting of the dataset (τ_{DA} = 391 ps when using τ_D = 1 ns).

T47D breast cancer cells were incubated for 1 hr with donor- and acceptor-labeled holo-Tf (Tf-AF700 and Tf-AF750) at different A:D ratios. After fixation, the cells were imaged with the time-gated FLI system and analyzed using both phFLI and standard decay fitting approaches. Figure 5C shows the phasor locations for different A:D ratios which, as in the previous experiment, appear aligned on a segment connecting the donor-only sample and an hypothetical maximally-quenched sample. Converting these locations into phasor ratios (or equivalently, FRET population fractions), the curve shown in figure 5D (black squares) is obtained, which confirms the trend obtained by standard decay fitting (red circles), and corresponds to the expected asymptotic saturation predicted by the simple model described in supplementary note 5 (dashed curves).

3.4 Quantification of *in vivo* FRET dynamics

Having validated the use of phasor analysis with NIR FRET *in vitro*, we examined whether a similar type of analysis would be possible *in vivo*. While *in vivo* NIR fluorescence lifetime imaging is essentially devoid of background autofluorescence, it is complicated by light scattering and absorption by tissues, which broaden the temporal response and attenuate the signal intensity[50,51]. Since these effects

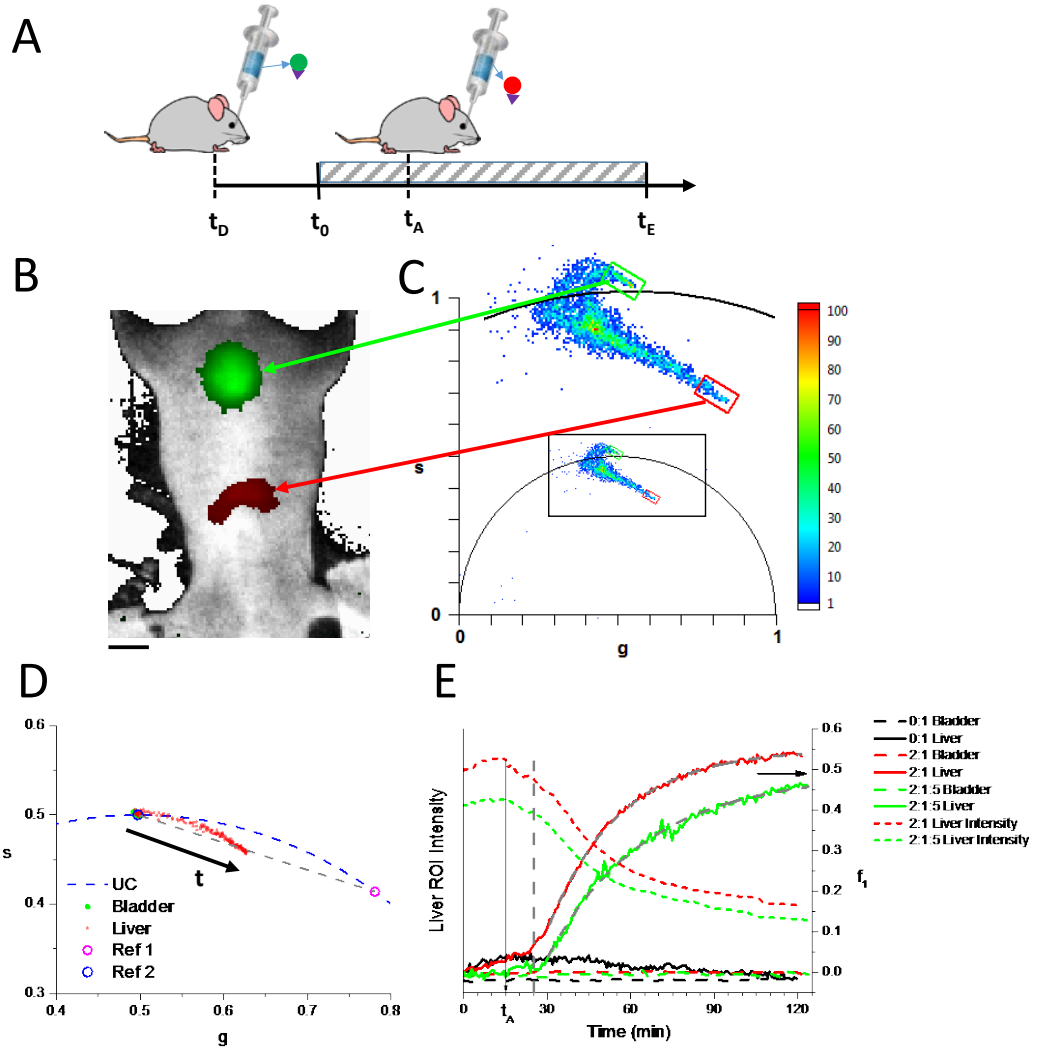

Figure 6: *in vivo* kinetics of transferrin engagement with Tf-receptor. A: principle of the experiment. Mice were first injected with Tf-AF700 (time t_D), and imaging started after several minutes (time t_0). 15 min after the beginning of the imaging session, Tf-AF750 was injected (time t_A) and imaging continued for another 1.45 hr. B: White light image of an anesthetized mouse (2:1:5) about half-way through the imaging session. The bladder (top, green) and liver (bottom, red) are highlighted by selection of two localized regions in the phasor plot shown in C. C: Phasor plot (and detail of the boxed area), with two rectangle ROIs selecting particular regions of the plot. D: Phasor plot showing the loci of the bladder ROI's average phasor (green dots) and liver ROI's average phasor (red dots) over the duration of the whole experiment. The references used for phasor ratio calibration are indicated as Ref 1 (0.53 ns) and Ref 2 (1 ns). E: Liver ROI intensity (left) and phasor ratio f_1 (right) for (1) a control mouse without Tf-AF750 injection (0:1: black), (2) a mouse injected with 2:1 Tf-AF750 injection at t_A = 15 min (2:1: red) and (3) a mouse injected with 2:1 Tf-AF750 and 5:1 unlabeled Tf at t_A (2:1:5: green). Short dashed curves represent the liver ROI intensity, dashed curves correspond to the bladder phasor ratio, while plain curves of the same color correspond to the liver phasor ratio. Gray dashed curves are exponential fits of the experimental curves (for t > 30 min) with $\tau_{2:1}$ = 1,528 ± 15 s and $\tau_{2:1:5}$ = 2,109 ± 55 s. The vertical arrow indicates t_A. The vertical dashed line is a guide for the eye indicating the onset of phasor ratio increase. See supplementary movie 2 for an animation of panel B &C.

are strongly depth-dependent, animal respiration, which periodically affects the depth of some organs such as the liver, could potentially complicate the analysis. Finally, a fraction of injected fluorescent molecule is initially non-specifically distributed throughout the body, potentially obfuscating the analysis.

We have previously demonstrated that *in vivo* FLIM FRET imaging of intravenously injected donor- and acceptor-labeled holo-Tf in anesthetized mice bearing tumor xenografts, allows monitoring TfR engagement by Tf[23]. In these studies, we measured detectable accumulation of doubly-labeled TfR in tumors at 1 hr post-injection based on double-exponential fitting of observed decays. We later used the same animal model system to demonstrate the advantages of adaptive wide field illumination (AWFI) to quantify receptor engagement at 6 and 24 hr post-injection in organs with high endogenous levels of TfR expression such as the liver and kidneys[52]. Here, we focused our study on the early time scale (0-2 hr) post intravenous injection, and performed *continuous* time-gated fluorescence imaging of the injected Tf-AF700, in order to investigate the initial kinetics of non-specific accumulation of Tf in the liver, as well as its elimination in the bladder. Donor- (AF700) and acceptor- (AF750) labeled holo-Tf were injected retro-orbitally in anesthetized mice at distinct time points separated by approximately 15 minutes (figure 6A). Mice injected with

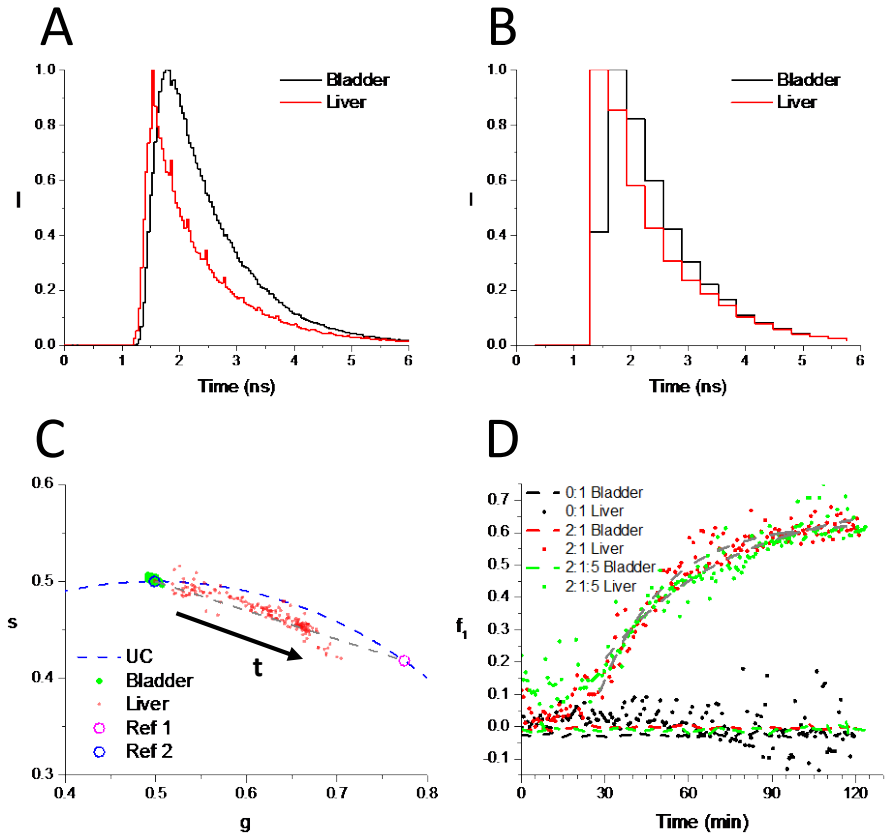

Figure 7: *in vivo* kinetics of transferrin engagement with Tf-receptor using a reduced number of gates. A: Example of full decay (168 gates) obtained in the bladder (black) and liver (red) of mouse 2:1:5. The spikes in the liver decay are due to the mouse's 0.7 Hz breathing pattern and reflect the sensitivity of the signal to source depth. B: Same decays as in A, represented with a subset of 20 contiguous gates. These coarse resolution decays were used for the remainder of the analysis. C: Detail of the corresponding phasor plots. Compare with the phasor plot obtained using all gates in Fig. 6D. Ref 1 and 2 where defined using the reprocessed data. D: Bladder and liver phasor ratio (f_1) plots for 3 mice. Dashed curves correspond to the bladder's phasor ratio, while dotted curves of the same color correspond to the liver phasor ratio. Gray dashed curves are exponential fits of the experimental curves (for $t > t_A$) with $\tau_{2:1} = 1{,}418 \pm 93$ s and $\tau_{2:1:5} = 2{,}769 \pm 356$ s. Notice that the asymptotic values are different than those obtained with the full set of gates (Fig. 6E), due to the different definitions of the short lifetime intersection (reference 1). Using the same references in both analyses would have resulted in similar asymptotic values.

an A:D ratio of 0:1 (no acceptor-labeled Tf) were used as control. An A:D ratio of 2:1, determined to be sufficient to observe TfR engagement in our previous studies[23,52], was used for the other experiments (figure 6). Donor FLI acquisition was performed every ~45 seconds over ~2 hours and data was analyzed by phFLI analysis and standard decay fitting analysis as described in supplementary methods. Figure 6B shows the fluorescence intensity image for one of the 2:1 mice in the middle of the measurement and figure 6C the corresponding phasor plot. It is immediately apparent that the distribution of phasors in a live mouse is more complex than that observed in the previously described *in vitro* experiments. It is however straightforward to find the original locations of specific phasors: phasors located toward the top of the universal circle (green rectangle in figure 6C) originate from the bladder region (green overlay in figure 6B), while phasors located toward the short lifetime region (red rectangle in figure 6C) originate from the liver (red overlay in figure 6B), where overexpression of TfR allows formation of donor-acceptor-labeled Tf pairs resulting in FRET (shorter lifetimes). The remainder of phasor values correspond to other locations in the animal in which circulating Tf-AF700 is found at diverse depth and in various local environments.

As shown in supplementary movie 2, color coding of the different phasor plot areas (long lifetime: green, short lifetime: red) allows qualitatively visualizing the progressive increase of the fraction of Tf-AF700 undergoing FRET with its AF750-labeled counterpart, without any fitting or sophisticated analysis. In addition to this qualitative use of the phasor plot, a quantitative analysis of the FRET fraction present in different regions of the mouse can be performed as in the *in vitro* examples discussed previously. Figure 6D shows the location of the averaged phasors of both bladder (green dots) and liver (red dots) at each time point during the measurement. While the calibrated bladder phasor stays approximately in the same location, the liver phasor slowly migrates towards a region of the phasor plot corresponding to shorter lifetimes. Natural reference points to study this evolution are the calibration phasor (single exponential decay, 1 ns, blue dot) and the extrapolation of the liver phasor "trajectory" to the universal circle (magenta dot). Computing the corresponding phasor ratios (short lifetime fraction, SI equation (SI-20)) for these two phasor populations (bladder and liver) result in curves shown in figure 6E. The mouse injected with donor-labeled Tf only (0:1) exhibits a fairly constant phasor ratio consistent with no significant fraction of Tf-AF700 bound together with Tf-AF50 to TfR. Mice injected successively with donor- and acceptor-labeled Tf (2:1 & 2:1:5), show distinct kinetic, characterized by an exponential increase of the short lifetime phasor component shortly (but not immediately) after injection. These trends are supported by standard decay fitting analysis (supplementary figure 3), but are here obtained without the complexity and processing time associated with that latter approach. Interestingly, the recorded donor-intensity in the liver decreases immediately after injection (short dashed curves in figure 6E), while lifetime analysis detects a delayed onset of donor quenching by Tf-AF50.

3.5 Checking the speed limit of phFLI

Having demonstrated the ability to detect subtle changes in molecular targeting in live mice by phasor analysis, we asked whether we could take advantage of the negligible computational cost of phFLI and its robustness with respect to decay temporal resolution[43], to speed up fluorescence lifetime analysis and enable real-time phFLI. To reduce the effective acquisition time, we reprocessed the data presented in figure 6 using only 1/8 of the time-gate images, keeping only non-overlapping gates covering the whole decay (figure 7A). The low resolution fluorescence decays obtained with this reduced number of gates (19 gates) is clearly insufficient for a meaningful analysis by bi-exponential fitting, but sufficient to compute individual pixel phasors and phasor ratios of regions of interest, as illustrated in figure 7B&C. These results are qualitatively comparable to those obtained using all 150 gates (figure 6D&E), demonstrating that an acquisition time 8-fold shorter (~4 s per time point) could have been used without significantly affecting phFLI analysis. A further 6-fold speed-up could in principle be obtained by reducing the integration time per gate (200 ms for the data shown in figure 6&7), down to the minimum frame duration of the camera (30 ms), as the

signal-to-noise ratio of these measurements was very high (single pixel: 47, whole ROI > 400). A 19-gate image could then be acquired in less than 1 s, providing data which could be processed by phFLI and represented in real-time.

4 Discussion

We have established that phasor analysis of time-gated lifetime images can measure minute changes in the lifetime of NIR dyes characterized by short intrinsic lifetimes *in vitro* (~20 ps over lifetimes < 1 ns). We have also verified that phasor analysis is able to quantify the composition of a mixture of fluorophores characterized by single-exponential decays *in vitro*, even when the dyes fluorescence lifetimes are comparable to the width of the instrument function (τ_{HITCI} = 356 ps, $FWHM_{IRF}$ ~ 250 ps). We then exploited these properties of phasor analysis to quantify molecular interactions by FRET in two *in vitro* experiments, involving respectively fluorescently labeled complementary antibodies in solution, and fluorescently labeled ligands of membrane receptors in cell cultures. The results obtained by phasor analysis were comparable to those obtained by classical fluorescence decay fitting analysis. Finally, we extended these studies to the much more challenging situation of *in vivo* imaging, where fluorescence intensity decays are affected by scattering and absorption in a complex and spatially variable manner. We showed that even in this complex system, phasor analysis can be performed fairly straightforwardly and provides semi-quantitative results in good agreement with those obtained by fluorescence lifetime fitting. Importantly, phasor results were obtained almost instantaneously and robustly, while fluorescence lifetime fitting analysis was both computationally intensive and sensitive to initial conditions.

The demonstration that phasor analysis can be extended to the NIR domain where lifetimes are short and comparable to the IRF width, and in particular to *in vivo* imaging has many important implications. In addition to a decrease in processing time by several orders of magnitude compared to global multiple lifetime fitting approaches needed for quantitative analysis of lifetime mixtures, the robustness of phasor analysis to coarse-graining will allow reducing the acquisition time and or excitation intensity accordingly, minimizing laser power requirement and animal or sample exposure, as well as improving the temporal resolution of kinetic measurements. While the system used in this study is limited to frame rates slightly better than 1 Hz due to camera sensitivity and readout rate, newer models of time-gated cameras using sCMOS sensors and more sensitive photocathodes should be capable of much faster frame rates, only limited by the signal to noise ratio of the recorded time-gate images.

In addition to this speed advantage, phasor analysis of *in vivo* NIR time-gated data also provides a practical approach to implementing multiplexed imaging using lifetime as a contrast mechanism. NIR fluorescent dyes have broad emission spectra that are difficult to spectrally un-mix, due to the complex interplay between wavelength-dependent absorption and scattering in tissues. While fluorescence intensity decays are affected by these tissue characteristics, the measurements presented here demonstrate that these effects can be effectively compensated with prior information on the expected location of individual species in the phasor plot. In particular, the visualization of Tf receptor engagement in the liver illustrated in supplementary movie 2, and performed with no other aid but graphical selection of regions of interests in the phasor plot, shows that two fluorescent species characterized by sufficiently different lifetimes (e.g. 0.5 ns and 1 ns) can be readily separated and quantified. Importantly, such identification does not require fluorescent species to be characterized by single-exponential decays. The combination of imaging speed and lifetime contrast capability could be advantageously used for image-guided surgery using NIR markers differing mainly by their lifetimes (e.g. ICG and IRDye-800CW).

The quantitative nature of phasor analysis also suggests that it could be used as a replacement to or as a first estimator for the time- and memory-intensive multi-exponential decay fitting approach used in multiplexed fluorescence lifetime tomography imaging[53,54]. Finally, while our experiments used a time-gated detection based on intensified camera, the same analysis could be performed with data acquired by time-

gated or time-resolved single-photon avalanche diode arrays[55] or time-resolved wide-field photon-counting imagers[56].

5 Acknowledgements

This work was supported by NIH grant R01 EB19443 (XI & MB). XM was supported in part by DOE grant DE-FC02-02ER63421. The support of Shimon Weiss, in whose lab part of this work was performed, is gratefully acknowledged.

6 Author Contributions

SJC, NS and AR performed experiments. SJC and XM performed phasor analysis. SJC and NS performed lifetime fitting analysis. MB, XI, XM designed the experiments. XM developed the theory and software. SJC and XM wrote the manuscript draft. All authors contributed to the manuscript.

7 References

1 James, M. L. & Gambhir, S. S. A Molecular Imaging Primer: Modalities, Imaging Agents, and Applications. *Physiol Rev* **92**, 897-965, doi:10.1152/physrev.00049.2010 (2012).
2 Kim, C., Favazza, C. & Wang, L. H. V. In Vivo Photoacoustic Tomography of Chemicals: High-Resolution Functional and Molecular Optical Imaging at New Depths. *Chem. Rev.* **110**, 2756-2782, doi:10.1021/cr900266s (2010).
3 Frangioni, J. V. In vivo near-infrared fluorescence imaging. *Curr Opin Chem Biol* **7**, 626-634, doi:10.1016/j.cbpa.2003.08.007 (2003).
4 Hilderbrand, S. A. & Weissleder, R. Near-infrared fluorescence: application to in vivo molecular imaging. *Curr Opin Chem Biol* **14**, 71-79, doi:10.1016/j.cbpa.2009.09.029 (2010).
5 Willmann, J. K., van Bruggen, N., Dinkelborg, L. M. & Gambhir, S. S. Molecular imaging in drug development. *Nat Rev Drug Discov* **7**, 591-607, doi:10.1038/nrd2290 (2008).
6 Osmonov, D. K. *et al.* Sensitivity and specificity of PET/CT regarding the detection of lymph node metastases in prostate cancer recurrence. *Springerplus* **3**, 340, doi:10.1186/2193-1801-3-340 (2014).
7 Ozturk, M. S. *et al.* Mesoscopic Fluorescence Molecular Tomography for Evaluating Engineered Tissues. *Ann Biomed Eng* **44**, 667-679, doi:10.1007/s10439-015-1511-4 (2016).
8 Ozturk, M. S., Rohrbach, D., Sunar, U. & Intes, X. Mesoscopic Fluorescence Tomography of a Photosensitizer (HPPH) 3D Biodistribution in Skin Cancer. *Acad Radiol* **21**, 271-280, doi:DOI 10.1016/j.acra.2013.11.009 (2014).
9 Danhier, F., Feron, O. & Preat, V. To exploit the tumor microenvironment: Passive and active tumor targeting of nanocarriers for anti-cancer drug delivery. *J Control Release* **148**, 135-146, doi:10.1016/j.jconrel.2010.08.027 (2010).
10 Fang, J., Nakamura, H. & Maeda, H. The EPR effect: Unique features of tumor blood vessels for drug delivery, factors involved, and limitations and augmentation of the effect. *Adv Drug Deliver Rev* **63**, 136-151, doi:10.1016/j.addr.2010.04.009 (2011).
11 Suhling, K., French, P. M. W. & Phillips, D. Time-resolved fluorescence microscopy. *Photoch Photobio Sci* **4**, 13-22, doi:10.1039/b412924p (2005).
12 Berezin, M. Y. & Achilefu, S. Fluorescence Lifetime Measurements and Biological Imaging. *Chem. Rev.* **110**, 2641-2684, doi:10.1021/cr900343z (2010).
13 Jares-Erijman, E. A. & Jovin, T. M. FRET imaging. *Nat Biotechnol* **21**, 1387-1395, doi:10.1038/nbt896 (2003).
14 Warren, S. *et al.* in *Optics in the Life Sciences.* MTh1C.5 (Optical Society of America).
15 Jacques, S. L. Optical properties of biological tissues: a review. *Phys Med Biol* **58**, R37-R61, doi:10.1088/0031-9155/58/11/R37 (2013).

16 Daniels, T. R., Delgado, T., Rodriguez, J. A., Helguera, G. & Penichet, M. L. The transferrin receptor part I: Biology and targeting with cytotoxic antibodies for the treatment of cancer. *Clin Immunol* **121**, 144-158, doi:10.1016/j.clim.2006.06.010 (2006).
17 Daniels, T. R. *et al.* The transferrin receptor and the targeted delivery of therapeutic agents against cancer. *Biochimica Et Biophysica Acta* **1820**, 291-317, doi:10.1016/j.bbagen.2011.07.016 (2012).
18 Berczi, A., Barabas, K., Sizensky, J. A. & Faulk, W. P. Adriamycin Conjugates of Human Transferrin Bind Transferrin Receptors and Kill K562 and Hl-60-Cells. *Arch Biochem Biophys* **300**, 356-363, doi:DOI 10.1006/abbi.1993.1048 (1993).
19 Weaver, M. & Laske, D. W. Transferrin receptor ligand-targeted toxin conjugate (Tf-CRM107) for therapy of malignant gliomas. *J Neuro-Oncol* **65**, 3-13, doi:10.1023/A:1026246500788 (2003).
20 Wallrabe, H., Bonamy, G., Periasamy, A. & Barroso, M. Receptor complexes cotransported via polarized endocytic pathways form clusters with distinct organizations. *Mol Biol Cell* **18**, 2226-2243, doi:10.1091/mbc.E06-08-0700 (2007).
21 Talati, R. *et al.* Automated selection of regions of interest for intensity-based FRET analysis of transferrin endocytic trafficking in normal vs. cancer cells. *Methods* **66**, 139-152, doi:10.1016/j.ymeth.2013.08.017 (2014).
22 Abe, K., Zhao, L., Intes, X. & Barroso, M. in *Imaging and Applied Optics.* QTu3G.5 (Optical Society of America).
23 Abe, K., Zhao, L. L., Periasamy, A., Intes, X. & Barroso, M. Non-Invasive In Vivo Imaging of Near Infrared-labeled Transferrin in Breast Cancer Cells and Tumors Using Fluorescence Lifetime FRET. *Plos One* **8**, e80269, doi:10.1371/journal.pone.0080269 (2013).
24 Rudkouskaya, A. *et al.* Quantitative Imaging of Receptor-Ligand Engagement in Intact Live Animals. *bioRxiv*, 2017/2012/2003/228072, doi:10.1101/228072 (2017).
25 Akers, W. J., Berezin, M. Y., Lee, H. & Achilefu, S. Predicting in vivo fluorescence lifetime behavior of near-infrared fluorescent contrast agents using in vitro measurements. *J Biomed Opt* **13**, 054042, doi:10.1117/1.2982535 (2008).
26 Becker, W. *Advanced time-correlated single photon couting techniques*. (Springer, 2005).
27 Heeg, B. Precision of mono-exponential decay estimates from rapid lifetime determination in the presence of signal photon and background noise. *Meas Sci Technol* **25**, 105201, doi:10.1088/0957-0233/25/10/105201 (2014).
28 Leray, A., Padilla-Parra, S., Roul, J., Heliot, L. & Tramier, M. Spatio-Temporal Quantification of FRET in Living Cells by Fast Time-Domain FLIM: A Comparative Study of Non-Fitting Methods. *Plos One* **8**, e69335, doi:10.1371/journal.pone.0069335 (2013).
29 Padilla-Parra, S., Auduge, N., Coppey-Moisan, M. & Tramier, M. Non fitting based FRET–FLIM analysis approaches applied to quantify protein–protein interactions in live cells. *Biophysical Reviews* **3**, 63-70, doi:10.1007/s12551-011-0047-6 (2011).
30 Jameson, D. M., Gratton, E. & Hall, R. D. The Measurement and Analysis of Heterogeneous Emissions by Multifrequency Phase and Modulation Fluorometry. *Appl Spectrosc Rev* **20**, 55-106, doi:10.1080/05704928408081716 (1984).
31 Redford, G. I. & Clegg, R. M. Polar plot representation for frequency-domain analysis of fluorescence lifetimes. *J Fluoresc* **15**, 805-815, doi:10.1007/s10895-005-2990-8 (2005).
32 Weber, G. Resolution of the Fluorescence Lifetimes in a Heterogeneous System by Phase and Modulation Measurements. *J Phys Chem-Us* **85**, 949-953, doi:10.1021/j150608a006 (1981).
33 Digman, M. A., Caiolfa, V. R., Zamai, M. & Gratton, E. The phasor approach to fluorescence lifetime imaging analysis. *Biophys J* **94**, L14-L16, doi:10.1529/biophysj.107.120154 (2008).
34 Fereidouni, F., Esposito, A., Blab, G. A. & Gerritsen, H. C. A modified phasor approach for analyzing time-gated fluorescence lifetime images. *Journal of microscopy* **244**, 248-258, doi:10.1111/j.1365-2818.2011.03533.x (2011).
35 James, N. G., Ross, J. A., Stefl, M. & Jameson, D. M. Applications of phasor plots to in vitro protein studies. *Anal Biochem* **410**, 70-76, doi:10.1016/j.ab.2010.11.011 (2011).

36 Jameson, D. M., Vetromile, C. M. & James, N. G. Investigations of protein-protein interactions using time-resolved fluorescence and phasors. *Methods* **59**, 278-286, doi:10.1016/j.ymeth.2013.01.004 (2013).
37 Szmacinski, H., Toshchakov, V. & Lakowicz, J. R. Application of phasor plot and autofluorescence correction for study of heterogeneous cell population. *J Biomed Opt* **19**, 046017, doi:10.1117/1.Jbo.19.4.046017 (2014).
38 Stringari, C. *et al.* Phasor approach to fluorescence lifetime microscopy distinguishes different metabolic states of germ cells in a live tissue. *P Natl Acad Sci USA* **108**, 13582-13587, doi:10.1073/pnas.1108161108 (2011).
39 Xiao, A., Gibbons, A. E., Luker, K. E. & Luker, G. D. Fluorescence Lifetime Imaging of Apoptosis. *Tomography* **1**, 115-124, doi:10.18383/j.tom.2015.00163 (2015).
40 Hinde, E., Digman, M. A., Hahn, K. M. & Gratton, E. Millisecond spatiotemporal dynamics of FRET biosensors by the pair correlation function and the phasor approach to FLIM. *P Natl Acad Sci USA* **110**, 135-140, doi:10.1073/pnas.1211882110 (2013).
41 Clayton, A. H. A., Hanley, Q. S. & Verveer, P. J. Graphical representation and multicomponent analysis of single-frequency fluorescence lifetime imaging microscopy data. *Journal of microscopy* **213**, 1-5, doi:10.1111/j.1365-2818.2004.01265.x (2004).
42 Colyer, R. A. *et al.* Phasor imaging with a widefield photon-counting detector. *J Biomed Opt* **17**, 016008, doi:10.1117/1.Jbo.17.1.016008 (2012).
43 Colyer, R. A., Lee, C. & Gratton, E. A novel fluorescence lifetime imaging system that optimizes photon efficiency. *Microsc Res Techniq* **71**, 201-213, doi:10.1002/jemt.20540 (2008).
44 Venugopal, V., Chen, J. & Intes, X. Development of an optical imaging platform for functional imaging of small animals using wide-field excitation. *Biomed Opt Express* **1**, 143-156 (2010).
45 Furstenberg, A. Water in Biomolecular Fluorescence Spectroscopy and Imaging: Side Effects and Remedies. *Chimia* **71**, 26-31, doi:10.2533/chimia.2017.26 (2017).
46 Lee, S. F., Verolet, Q. & Furstenberg, A. Improved super-resolution microscopy with oxazine fluorophores in heavy water. *Angew Chem Int Ed Engl* **52**, 8948-8951, doi:10.1002/anie.201302341 (2013).
47 de Jong, L. A. A., Uges, D. R. A., Franke, J. P. & Bischoff, R. Receptor-ligand binding assays: Technologies and applications. *Journal of Chromatography B* **829**, 1-25, doi:10.1016/j.jchromb.2005.10.002 (2005).
48 Goddard, A. D. & Watts, A. Contributions of fluorescence techniques to understanding G protein-coupled receptor dimerisation. *Biophysical Reviews* **4**, 291-298, doi:10.1007/s12551-012-0073-z (2012).
49 Qian, Z. M., Li, H. Y., Sun, H. Z. & Ho, K. Targeted drug delivery via the transferrin receptor-mediated endocytosis pathway. *Pharmacol Rev* **54**, 561-587, doi:10.1124/pr.54.4.561 (2002).
50 Cormier, J. F. *et al.* The effects of self-absorption and detection geometry on fluorescence intensity and decay lifetime. *Optical Diagnostics and Sensing V* **5702**, 123-134, doi:10.1007/12.591026 (2005).
51 Hutchinson, C. L., Troy, T. L. & Sevick-Muraca, E. M. Fluorescence-lifetime determination in tissues or other scattering media from measurement of excitation and emission kinetics. *Appl Optics* **35**, 2325-2332, doi:10.1364/Ao.35.002325 (1996).
52 Zhao, L. L. *et al.* Spatial light modulator based active wide-field illumination for ex vivo and in vivo quantitative NIR FRET imaging. *Biomed Opt Express* **5**, 944-960, doi:10.1364/Boe.5.000944 (2014).
53 Venugopal, V., Chen, J., Barroso, M. & Intes, X. Quantitative tomographic imaging of intermolecular FRET in small animals. *Biomed Opt Express* **3**, 3161-3175, doi:10.1364/BOE.3.003161 (2012).
54 Venugopal, V., Chen, J., Lesage, F. & Intes, X. Full-field time-resolved fluorescence tomography of small animals. *Opt Lett* **35**, 3189-3191, doi:10.1364/OL.35.003189 (2010).

55 Bruschini, C., Homulle, H. & Charbon, E. Ten years of biophotonics single-photon SPAD imager applications - retrospective and outlook. *Proceedings of SPIE* **10069**, 10069S, doi:10.1117/12.2256247 (2017).
56 Colyer, R. A. *et al.* Phasor Analysis with a New Widefield Photon-Counting FLIM Detector. *Biophys J* **102**, 202a-202a (2012).
57 Zhao, L. L., Abe, K., Barroso, M. & Intes, X. Active wide-field illumination for high-throughput fluorescence lifetime imaging. *Opt Lett* **38**, 3976-3979, doi:10.1364/OL.38.003976 (2013).
58 Chen, S.-J., Sinsuebphon, N. & Intes, X. Assessment of Gate Width Size on Lifetime-based Förster Resonance Energy Transfer Parameter Estimation. *Photonics* **2**, 1027-1042, doi:10.3390/photonics2041027 (2015).
59 Myszka, D. G., He, X., Dembo, M., Morton, T. A. & Goldstein, B. Extending the range of rate constants available from BIACORE: Interpreting mass transport-influenced binding data. *Biophys J* **75**, 583-594, doi:10.1016/S0006-3495(98)77549-6 (1998).
60 West, A. P. *et al.* Comparison of the interactions of transferrin receptor and transferrin receptor 2 with transferrin and the hereditary hemochromatosis protein HFE. *J Biol Chem* **275**, 38135-38138, doi:10.1074/jbc.C000664200 (2000).
61 Inoue, T., Cavanaugh, P. G., Steck, P. A., Brunner, N. & Nicolson, G. L. Differences in Transferrin Response and Numbers of Transferrin Receptors in Rat and Human Mammary-Carcinoma Lines of Different Metastatic Potentials. *J Cell Physiol* **156**, 212-217, doi:10.1002/jcp.1041560128 (1993).